applied sciences

MDPI

Article

Dynamic Analysis of a High-Performance Prosthetic Leg: Experimental Characterisation and Numerical Modelling

Claudia Barattini, Luca Dimauro, Angelo Domenico Vella * and Alessandro Vigliani

Department of Mechanical and Aerospace Engineering, Politecnico di Torino, Corso Duca degli Abruzzi 24, 10129 Torino, Italy; claudia.barattini@polito.it (C.B.); luca.dimauro@polito.it (L.D.); alessandro.vigliani@polito.it (A.V.)

* Correspondence: angelo.vella@polito.it; Tel.: +39-340-051-7389

Abstract: In recent years, significant improvements in the design of leg blade prosthetics have been carried out. After several advances in material and topological optimisations, sport-purpose feet prosthetics have reached high-level performances, allowing athletes with limb loss to participate in various sport activities at a competitive level. Since the knowledge of prosthetic mechanical behaviour is crucial for its optimal design, specific studies are required to meet the anthropometric characteristics of the athlete. This research work is focused on investigating the dynamic behaviour of a running blade prosthetic and developing a validated prosthetic model, placing particular emphasis on the definition of suitable material properties. An experimental modal analysis is performed on the Cheetah Xcel, Össur lower limb prosthetic. In contrast with what has already been presented in the literature, a roving hummer test under free–free conditions is proposed here to avoid the uncertainties due to constraint conditions. For the first time, blade prosthetic dynamic characteristics in free–free conditions are presented. Additionally, a novel Finite Element model of the prosthetic is developed and tuned on the basis of the experimental results. The modal assurance criterion index is exploited to compare experimental and numerical mode shapes. Starting from frequency response functions, the first six mode shapes are experimentally identified in the frequency range up to 750 Hz, including both bending and torsion. As expected, the bending in the vertical plane constitutes the primary mode shape: this kind of flexion enhances energy storage, enabling athletes to achieve an optimal running gait. This study shows the dynamic modal behaviour of a lower limb prosthetic in free–free conditions and demonstrates that a traditional isotropic material is not suitable in describing its dynamic features. The development of a model that exploits orthotropic material properties improves the alignment between experimental and numerical outcomes. This result is in agreement with the material composition of the prosthetic, which consists of carbon fibre layers.

Keywords: lower limb prosthetic leg; modal analysis; numerical–experimental correlation; orthotropic material; composite prosthetic; carbon fibre and epoxy matrix

Citation: Barattini, C.; Dimauro, L.; Vella, A.D.; Vigliani, A. Dynamic Analysis of a High-Performance Prosthetic Leg: Experimental Characterisation and Numerical Modelling. *Appl. Sci.* **2023**, *13*, 11566. https://doi.org/10.3390/app132011566

Academic Editor: Marek Krawczuk

Received: 25 September 2023
Revised: 18 October 2023
Accepted: 19 October 2023
Published: 23 October 2023

1. Introduction

In recent years, the introduction of advanced materials and innovative designs has led to the creation of Energy Storing And Return (ESAR) prosthetic feet, which better replicate the natural functions of the limb, given the improved energy storage and return properties [1]. The ESAR feet are typically made of carbon fibre composites due to their light weight, exceptional strength, and good chemical properties, which contribute to the component's durability. Additionally, they exhibit minimal deformation under varying loads compared to materials like aluminium and titanium alloys [2], and they provide a good spring-like [3,4] effect. Such prosthetics also confer better symmetry to the gait and they improve the subject's comfort and reactivity [5]. Last but not least, an important advantage of composite materials is that they can be "tailor made", allowing for precise

control over the mechanical behaviour of the components [6–8]. Improvements in prosthetic technology have led to the development of specialised sport-purpose feet, the blade prostheses [9–11]. These ESAR feet are specifically optimised for high-level sports, fulfilling the unique demands and requirements of athletes. They provide improved performance, stability, and responsiveness, allowing athletes with limb loss to engage in different sports activities at a competitive level.

Several studies proposed advances [12], challenges [13,14], and future perspectives [15] on lower limb prosthetic technology since the insight of its mechanical behaviour is essential for their proper design, development, and customisation, to optimally meet individual requirements [16]. Different research works can be found in the literature, treating various topics, such as static analysis of prosthesis technology used in elite sport [17,18] or for running [19–21], in order to evaluate the stiffness characteristics [22] of blade prosthetics, or the investigation of their dynamic performance [23,24]; other studies propose the development of wearable sensors for mapping the behaviour of energy storing and returning in prosthesis [25,26], and the assessment of the influence of different composite material in the performance of athletes with prostheses [8,27,28]. Indeed, no standardised tests are currently available to achieve a full characterisation of the mechanical behaviour of the blade prosthetic in operating conditions [29]. As pointed out from the research of Beck et al. [20,21], the running prostheses stiffness is affected by multiple factors. Indeed, when the speed increases from 3 m/s, the stiffness decreases. Furthermore, the dimension of the prosthetic affects the proximal bending moment value and thus the vertical displacement, resulting in different stiffness values. Above all, due to conflicting evidence in the literature and the insufficient information provided by the manufacturers, it is uncertain if the force–displacement profile is considered linear or curvilinear. For example, the mechanical tests of Dyer et al. [19] on Elite Blade prostheses demonstrate that the stiffness is load-dependent. The knowledge of the stiffness behaviour in correspondence to the peak of the force is important to understand the component performance, but its dynamic modal analysis also plays a pivotal role in unravelling the intricate mechanical and performance characteristics of the prosthetic devices. This analysis implies the identification and examination of the natural frequencies, mode shapes, and damping ratios of the foot blade prosthetics. Few works have been conducted with this purpose [30–36].

The correlation between the dynamic behaviour of prosthetic blades with the mass they carry is explored in [31,33]. Both studies employed a T-shaped steel mounting bracket to apply the masses to the prosthetics. The bracket was carefully fixed to ensure that the line of action of the masses aligned with the ground reaction point of the foot, preventing any rotational effects. The researchers found out that the natural frequencies increase with stiffer prosthetic categories. They concluded that the foot should not be merely prescribed based on the weight of the amputees but also based on their activity level so as to reach the first bending natural frequency of the component and thus achieve enhanced performances. The first four eigenmodes observed in these studies ([31,33]) are twisting and bending modes, which could be excited by impacts such as those occurring when jumping, walking, or running. The first bending mode, contributing to vertical displacement, is found to be significant in this process. Twisting modes occur close to or before the first bending mode, indicating an elastic coupling between bending and twisting. Factors like asymmetrical loading, section asymmetry, or shear coupling due to material anisotropy influenced this behaviour. Despite observing non-linearities, the researchers concluded that approximating the stiffness as linear could closely predict the frequency of the first bending mode, irrespective of the mass or weight of the amputee, providing practical applications for selecting prosthetic stiffness based on gait performance requirements.

Nakayama et al. [34] provided insights into the rebound characteristics of running-specific prostheses. By applying an impactor on the blade prosthetic at different impact speeds, in order to simulate jogging, sprinting, and top athletes' contact speeds, it resulted that, as the impact speed increases, both load and displacements also increase. The ratio between the rebound and impact speeds shows significant variation with changes in the

model and impact speed, while the ratio between the maximum impact load and the correspondent displacement remains almost constant regardless of the impact speed.

Moreover, Rigney et al. [25] aimed to examine the feasibility of using Finite Element Analysis (FEA) to standardise the mechanical characterisation of ESAR feet, proposing a methodology that integrates numerical and experimental analysis. Two quasi-static tests were conducted on the prosthetic, exploiting an Instron tensile/compression testing machine in order to find out the Young modulus and the static and dynamic friction coefficient. Afterwards, the simulation of the dynamic loading response was also carried out and the Rayleigh parameters, stiffness, and energy efficiency were evaluated. From the dynamic loading response, it was possible to deduce that ESAR prostheses with high stiffness result in low energy loss but high impulse, potentially increasing the residual limb reaction force. The largest contributing factors to energy loss in dynamically loaded ESAR prostheses are shape and thickness.

These studies highlight the significance of conducting dynamic tests on blade prosthetics to gain a deeper understanding of their performance, thereby contributing to the improvement in the manufactured products.

Recently, researchers have also explored the potential of harvesting energy from the movement and mechanical forces experienced during walking or running [37–39]. This could be an important step for advancement in prosthetics technology since the harvested energy could be used to power various components of the prosthesis, such as motors, sensors, or microprocessors.

This paper presents the dynamic characterisation of the composite ESAR prosthetic feet Cheeta Xcel, Össur [40] through Experimental Modal Analysis (EMA). In contrast with previous studies, the experimental roving hammer test is performed in free–free conditions in order to avoid potential uncertainties associated with the applied loads and constraints. As underlined by the literature review, the dynamic characterisation of a prosthetic is generally conducted applying a vertical load and simulating the athlete weight [31,33] or by constraining the prosthetic area close to the socket [34]. These testing assumptions, which may help to study the system in real operative conditions, can lead to the evaluation of dynamic behaviour far from reality because of load misalignment and the vibrations of the clamping devices. In contrast, this research work aims at characterising the modal behaviour of the prosthetic as an independent system, avoiding sources of uncertainties. The proposed approach allows also to investigate the material properties of the prosthetic. To achieve this goal, a numerical Finite Element (FE) model is developed including an orthotropic material in line with the real component to obtain better agreement between experimental and numerical results.

The paper is organised as follows: in Section 2, the experimental setup adopted for the EMA is presented and the obtained results are outlined. Afterwards, in Section 3, the numerical model is introduced and the simulation results are compared with the experimental outcomes, proposing an updating of material properties. Finally, in Section 4, the conclusions are drawn and some considerations on possible future developments are presented.

2. Experimental Modal Analysis

A roving hammer test was performed on the blade prosthetic Cheetah Xcel, Össur [40]. Blade prostheses are produced in a range of stiffness values, divided into specified categories. The tested prosthetic belongs to category 6 and thus is intended for users from around 89 kg to 100 kg. The overall characteristics of the component are outlined in Table 1.

Table 1. Characteristics of Cheetah Xcel, Össur.

Product Weight	Max. System Height	Max. User Weight Suggested
1.036 kg	569 mm	100 kg

2.1. Sensors Setup

The prosthetic leg has been tested adopting free–free conditions by suspending the prosthetic with an elastic band. In Figure 1, the reference system considered in the experimental campaign is shown. The origin lies on the prosthetic plane of symmetry, at the midpoint of the width (attachment to the socket). The Y-axis is directed along the prosthetic width, while vertical Z-axis points downwards, towards the prosthetic toe.

The structure is excited using an impact hammer (PCB, sensitivity: 2.2 mV/N) with a medium hardness plastic tip. The selected node configuration for hammering consists of one central row aligned with the prosthetic plane of symmetry and two lateral rows, each containing 19 nodes spaced along the prosthetic shape, for a total number of 57 nodes. Their location has been previously chosen balancing geometry accuracy and expected modal behaviour. The nodes are hammered along all the possible directions allowed by the prosthetic shape, for a total number of 96 possible strokes. Indeed, the hammered directions must be orthogonal to the corresponding node surface. During the roving hammer test, all the nodes at the prosthetic side are excited both along the width (Y direction) and along the component shape.

Nodes nomenclature is based on the following considerations:

- middle line of prosthetic is numbered with 1XX;
- left side (Y+ surface) is numbered with 2XX;
- right side (Y− surface) is numbered with 3XX.

Five of the fifty-seven nodes identified to be hammered are even used as accelerometer locations. One mono-axial (PCB, sensitivity equal to 100 mV/g) and four tri-axial (PCB, sensitivity equal to 100 mV/g) accelerometers are used to evaluate system response, obtaining a total amount of 1248 Frequency Response Functions (FRFs). Details of their location are reported in Figure 2, while the reference geometry of the EMA test is displayed in Figure 3, in which the accelerometer positions are marked with coloured dots.

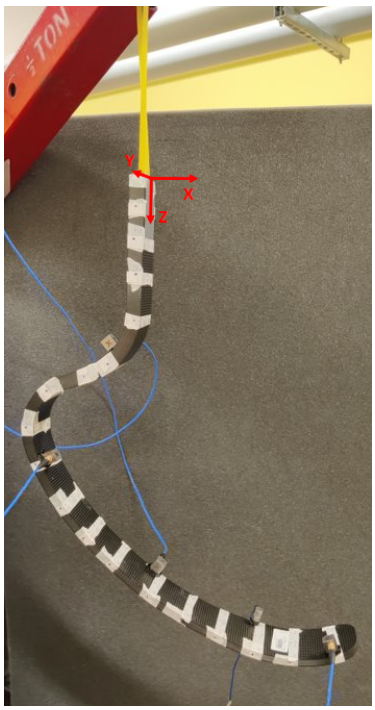

Figure 1. Experimental setup scenario.

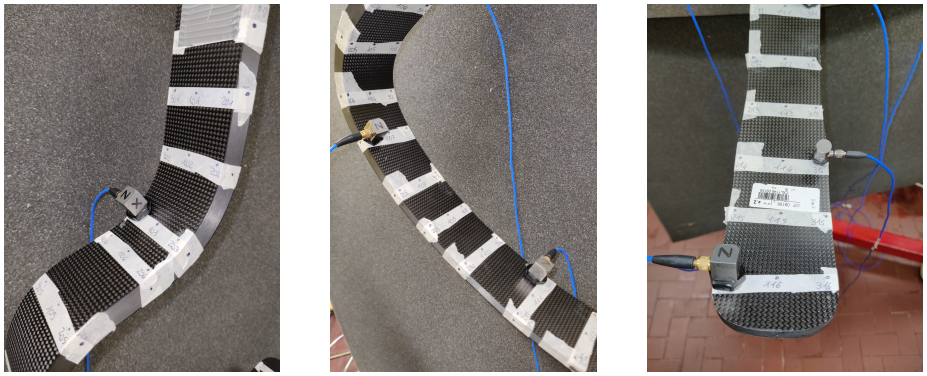

(**a**) (**b**) (**c**)

Figure 2. Details of the implemented hardware: referring to accelerometer nomenclature of Figure 3, tri-axial node 303 (**a**), tri-axial nodes 207 and 311 (**b**), tri-axial node 216 and mono-axial node 314 (**c**).

The excitation and response signals are acquired using Siemens LMS SCADAS Mobile acquisition device. To do so, LMS Test.Lab 17 software is used: time histories of 4 s (frequency resolution of 0.25 Hz) are acquired with a sampling frequency of 8192 Hz; force-exponential window is applied for the hammer input signal over 0.6% of samples, while exponential window with a decay of 30% is applied to accelerometer outputs; H_1 estimation of the system inertance FRFs is linearly averaged on 3 repetitions [41]. On Test.Lab software, the geometry definition requires the orientation each node (Euler angles). These angles are exploited to properly rotate the local reference frame of the hammered nodes with respect to the global reference frame of the component in order to obtain the correct hammering directions (orthogonal to the prosthetic surfaces).

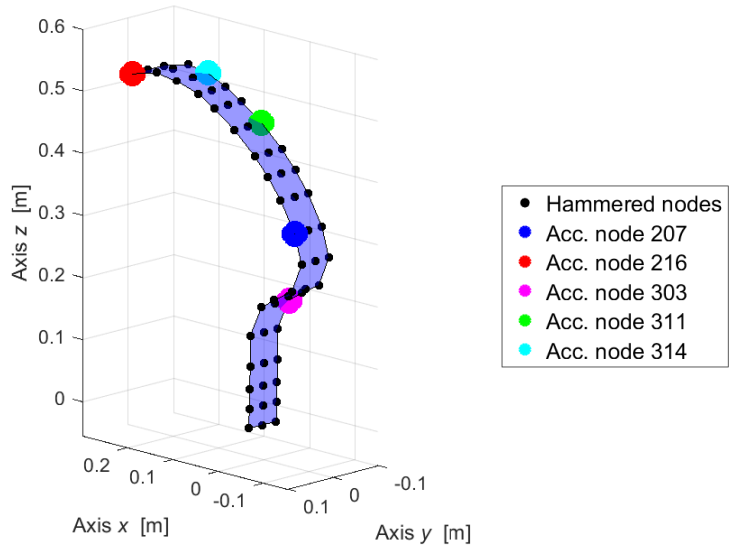

Figure 3. Reference geometry for experimental test.

2.2. Experimental Modal Analysis Results

The Experimental Modal Analysis (EMA) has been carried out to evaluate the modal properties of the prosthesis, i.e., the natural frequencies (f_r), damping ratios (ζ_r), and mode shapes ($\mathbf{\Phi}_r$), which are identified in the frequency range from 0 Hz to 750 Hz using PolyMAX algorithm [42], and 6 mode shapes are obtained (Table 2).

The reference system considered in the description of the mode shapes is the same described in Section 2.1, as illustrated in the plots of the experimental mode shapes (Figure 4).

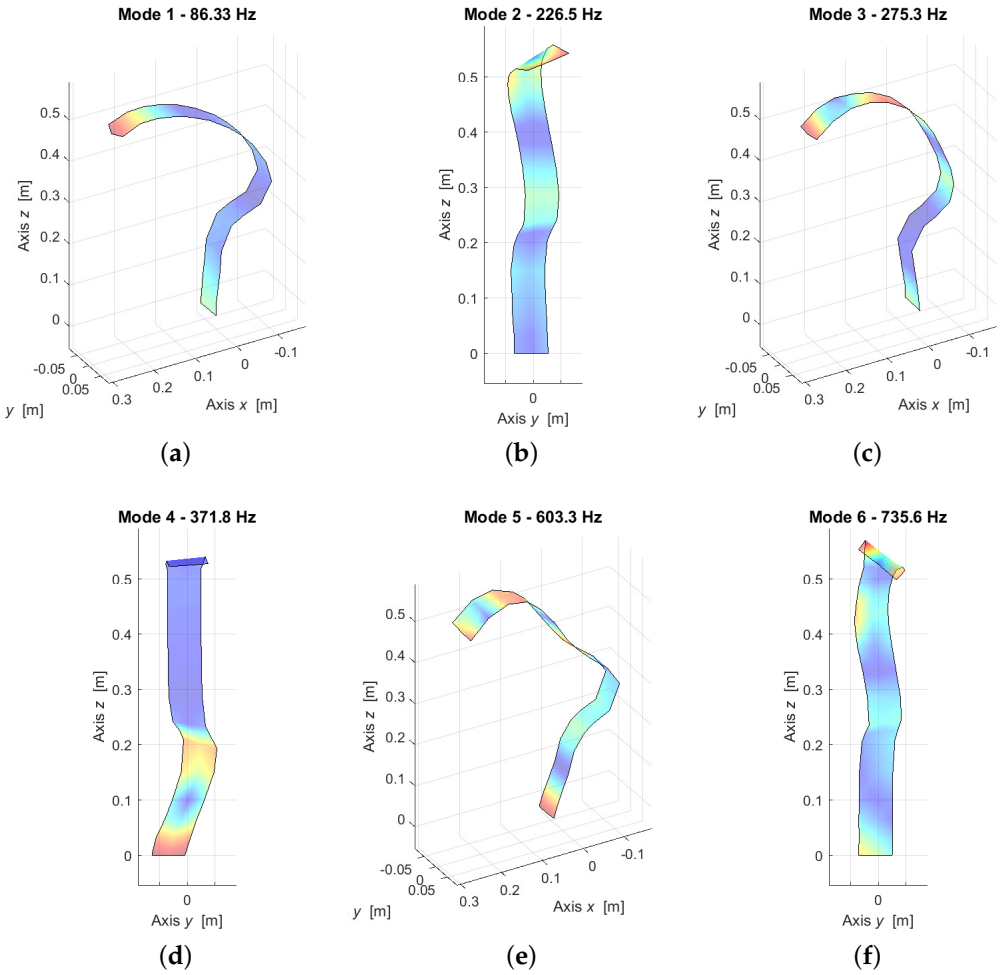

Figure 4. Experimental mode shapes plotted using LUPOS software.

Table 2. Natural frequencies (f_r) and damping ratios (ζ_r) identified in the frequency range from 0 Hz to 750 Hz.

Mode n.	f_r [Hz]	ζ_r [%]	Mode Type
1	86.33	0.38	1st bending XZ
2	226.49	1.06	Torsion RZ/1st bending XY
3	275.25	0.24	2nd bending XZ
4	371.77	0.41	Torsion RZ/2nd bending XY
5	603.34	0.48	3rd bending XZ
6	735.58	1.95	Torsion RZ/3rd bending XY

As clearly evident from the table, the principal mode shapes of the prosthetic are the bending in the XZ plane and the torsion around Z combined with bending in the XY plane. This is due to the prosthesis geometry since the thickness of the cross-section is less than the width in Y direction. Furthermore, it is reasonable to have as first mode the bending in the vertical plane since the limb prosthetic must deform along the Z direction in order to promote the storing and restoring energy function, helping athletes to perform the running gait.

In order to check the reliability of the results, the experimental (Exp) and the synthesised auto-inertance FRFs are compared, as shown in Figure 5. The synthesised ones are

obtained using the following two methods: using TestLab (Syn), where the identified modal set and both lower and upper residuals ($[LR]$ and $[UR]$) are considered, Eqaution (1) [42], and with the modal superposition (MS) principle, Equation (2), where no residuals are taken into account. In Equations (1) and (2), $A_{j,k}(\omega)$ is the inertance FRF computed for each ω between the two DoFs j and k, while ω_r and ζ_r are the natural frequency and the damping ratio of the r-th mode shape $\mathbf{\Phi}_k$. For the auto-inertances, the two DoFs are the same: $k = j$. For sake of clarity, the excited (E) and measured (R) nodes with their directions are mentioned in the title of each graph.

$$A_{j,k}(\omega) = \frac{\ddot{x}_j(\omega)}{F_k(\omega)} = -\omega^2 \frac{x_j(\omega)}{F_k(\omega)} = \sum_{r=1}^{n} \frac{-\omega^2 \; \Phi_{j,r} \, \Phi_{k,r}}{\omega_r^2 + 2\,\mathrm{i}\,\zeta_r \, \omega_r \, \omega - \omega^2} + [LR] - \omega^2 [UR] \tag{1}$$

$$A_{j,k}(\omega) = \frac{\ddot{x}_j(\omega)}{F_k(\omega)} = -\omega^2 \frac{x_j(\omega)}{F_k(\omega)} = \sum_{r=1}^{n} \frac{-\omega^2 \; \Phi_{j,r} \, \Phi_{k,r}}{\omega_r^2 + 2\,\mathrm{i}\,\zeta_r \, \omega_r \, \omega - \omega^2} \tag{2}$$

As clearly visible in Figure 5, really good agreement between the auto-inertances is obtained for nodes 207 and 303 in the frequency range between 0 Hz and 400 Hz. Furthermore, the synthesised auto-inertance values resulting from TestLab are closer to the experimental outcomes. Indeed, they are more reliable with respect to the modal superposition calculus since, in the first computation model, both lower and upper residuals are considered.

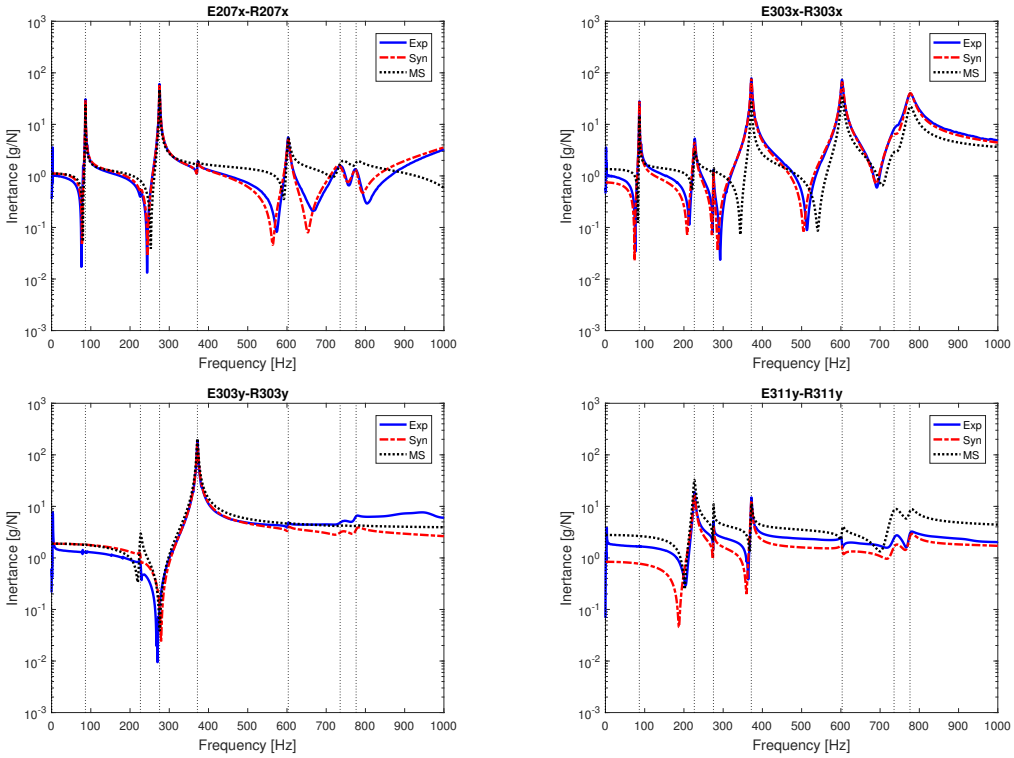

Figure 5. Auto-inertance FRFs: experimental (blue solid line), TestLab-synthetised (red dash–dot line), and synthetised with modal superposition (black dot curve).

The linearity of the component is then verified by analysing the Maxwell reciprocity. The reciprocity test is performed by plotting the cross-inertances, switching the excited and measured nodes and directions, as shown in Figure 6.

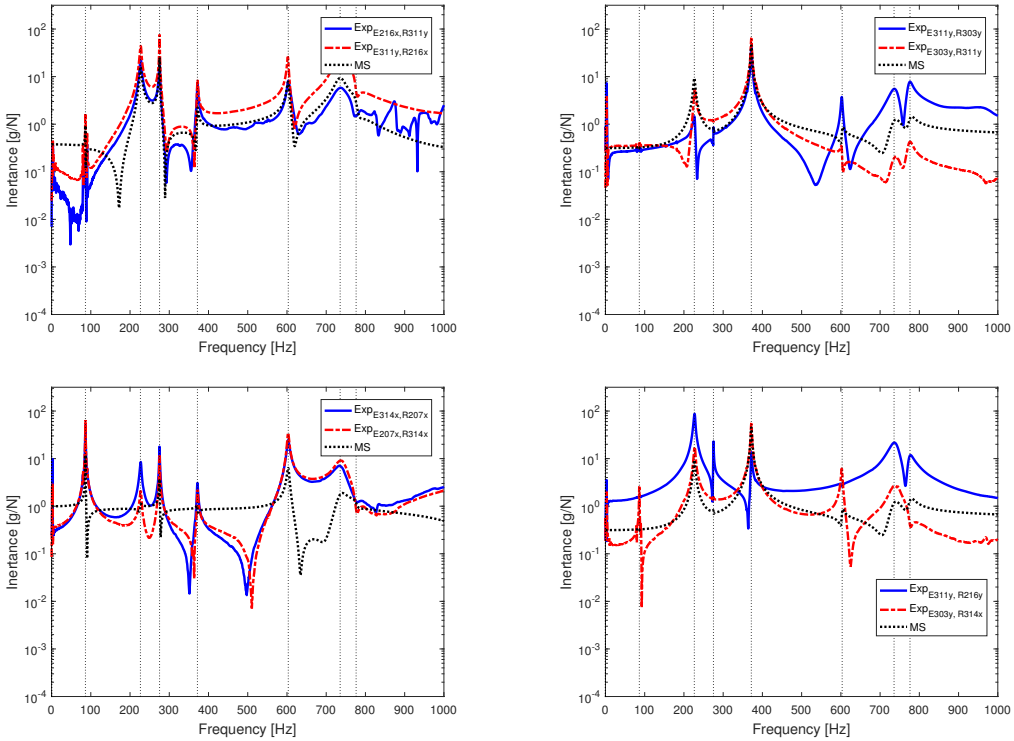

Figure 6. Maxwell reciprocity test: experimental cross-inertance FRFs comparison interchanging excited (E) and measured (R) nodes and directions. Cross-inertance calculated using the modal superposition principle (Equation (2)) in black dot.

3. Numerical Modelling

The FE models are developed using LUPOS 2023 software [43], namely a LUmped Parameter Open Source FEM code developed in Matlab, and real modal analysis is computed with MSC Nastran 2017.

The prosthetic is discretised with 3D hexagonal elements (CHEXA). The characteristics of the resulting model are presented in Table 3, where the number of elements along the thickness and the width directions are also reported. The model is displayed in Figure 7. From the upper and lateral views of the image, it is clearly visible that gradual changes along the width and thickness dimensions of the real prosthetic are well discretised.

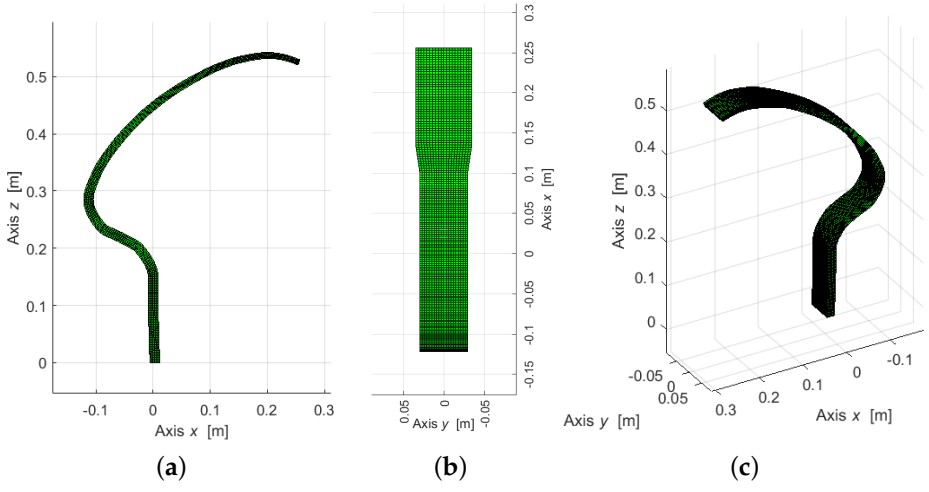

Figure 7. 3D LUPOS FEM model of the foot blade prosthetic: lateral (**a**), top (**b**), and isometric (**c**) views.

Table 3. Characteristics of the 3D model.

Nodes	40,131
Elements	32,640
DoFs	240,786
Hexa along the thickness	6
Hexa along the width	20

The same free–free conditions of the experimental test have been considered; thus, the model has not been constrained. Firstly, the material is considered isotropic, and its properties are reported in Table 4. The density is calculated knowing the weight and volume of the component. The weight is experimentally measured, while the volume is deduced from the prosthetic shape creation on the 3D CAD software SolidWorks 2015. The starting value of the Young modulus was 64.3 GPa, resulting from the static analysis performed by Rigney et al. [25] on the Cheetah Xtreme model, category 5. The numerical model has been tuned by adjusting the values of the Poisson ratio and the Young modulus to achieve a closer match with the experimental natural frequencies. The tuning procedure for the isotropic material was performed considering that the Young modulus scales equally all the natural frequencies since it is related to the stiffness. On the other hand, the Poisson ratio has effects on the relation between torsional and bending modes since it is the only parameter that affects the eigenvalues related to different mode shapes differently. Performing a parametric analysis on the Poisson ratio, it is noticed that the torsional modes are more sensitive to its variation with respect to bending ones. In detail, by varying the Poisson ratio from 0.15 to 0.45, the bending natural frequencies values slightly increase, while the torsional ones decrease by a major factor. Consequently, a Poisson ratio of 0.45 is selected to achieve the lowest natural frequency values for torsional modes and the highest for bending modes.

The correspondence between numerical and experimental results is also performed by evaluating the Modal Assurance Criterion (MAC) between the simulated and experimental mode shapes (Equation (3)) [44]. It is an index that measures the correlation level between two mode shapes $\mathbf{\Phi}_j$ and $\mathbf{\Phi}_k$, respectively. It is defined as follows:

$$MAC_{j,k} = \frac{\left[\mathbf{\Phi}_j^T \, \mathbf{\Phi}_k\right]^2}{\left[\mathbf{\Phi}_j^T \, \mathbf{\Phi}_j\right] \left[\mathbf{\Phi}_k^T \, \mathbf{\Phi}_k\right]} \tag{3}$$

Given its definition, the MAC index is always positive, and its range is from zero to one. When two eigenvectors are orthogonal or have very low similarity, MAC is nil, while it tends to one when the two modes are equal. Two models show the same dynamic behaviour when the MAC matrix is the identity matrix.

Table 4. Isotropic material properties of the 3D model.

Property	**Value**
Density	1549 kg/m^3
Poisson ratio	0.45
Young modulus	32 GPa

Figure 8a represents the MAC between FEA and EMA results adopting an isotropic material for the model. The dashed line represents the iso-frequency curve. In this case, the MAC matrix is not diagonal. Indeed, besides the first mode shape, which is bending in the XZ plane, the mode order does not correspond between the numerical (FEA) and experimental results (EMA). This aspect is underlined by Table 5, where EMA and FEA (isotropic material) natural frequencies are compared, considering EMA mode ascending order.

In Table 5, MAC values between corresponding modes are also reported. The last two modes of Table 5 are characterised by a MAC index lower than 70%, which is here considered as benchmark [45] for eigenvectors agreement. Consequently, in the simulation, the fifth and the sixth EMA mode shapes are not accurately reproduced in FEA. Considering the discrepancy in terms of mode order between the FEA and EMA results, the assumption of isotropic material properties is not reliable in this case study. Therefore, an anisotropic material is introduced in the Finite Element model.

Table 5. Natural frequencies and MAC values between EMA and FEA (isotropic material): mode shapes are compared following the ascending order of EMA frequencies.

f_{FEA} [Hz]	f_{EMA} [Hz]	Mode Shape	MAC [%]
87.96	86.33	1st bending XZ	87.96
401.32	226.49	Torsion RZ/1st bending XY	79.76
263.94	275.25	2nd bending XZ	76.43
499.60	371.77	Torsion RZ/2nd bending XY	95.13
489.24	603.34	3rd bending XZ	57.74
1021.20	735.60	Torsion RZ/3rd bending XY	55.67

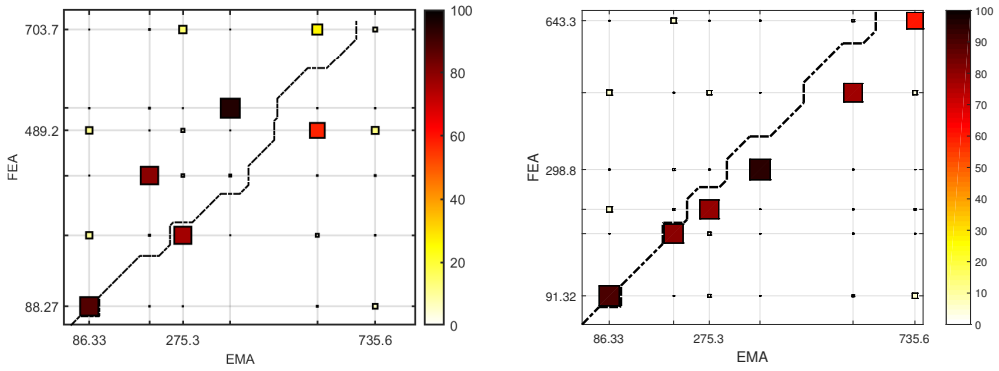

(**a**) (**b**)

Figure 8. MAC matrix, comparison between EMA and FEA results: isotropic (**a**) and orthotropic (**b**) models.

In Nastran, for linear structural analyses, the MAT9 definition [46] allows to assign orthotropic material properties to 3D solid elements. Since the prosthetic material is carbon fibre composite, the definition of orthotropic properties is reasonable [47–49]. The fibres confer strength along their length, meaning that the orientation and length of the fibres directly influence the behaviour of the composite material. In this case, the internal composition of the prosthetic was disclosed by Össur company.

Therefore, for simplicity, the material is not defined layer by layer, but the overall properties along the local reference frame of each element are considered. The stress–strain deformation for an orthotropic material follows Equation (4) [50]:

$$\begin{Bmatrix} \varepsilon_1 \\ \varepsilon_2 \\ \varepsilon_3 \\ \gamma_{23} \\ \gamma_{31} \\ \gamma_{12} \end{Bmatrix} = \begin{bmatrix} \frac{1}{E_1} & -\frac{\nu_{21}}{E_2} & -\frac{\nu_{31}}{E_3} & 0 & 0 & 0 \\ -\frac{\nu_{12}}{E_1} & \frac{1}{E_2} & -\frac{\nu_{32}}{E_3} & 0 & 0 & 0 \\ -\frac{\nu_{13}}{E_1} & -\frac{\nu_{23}}{E_2} & \frac{1}{E_3} & 0 & 0 & 0 \\ 0 & 0 & 0 & \frac{1}{G_{23}} & 0 & 0 \\ 0 & 0 & 0 & 0 & \frac{1}{G_{13}} & 0 \\ 0 & 0 & 0 & 0 & 0 & \frac{1}{G_{12}} \end{bmatrix} \cdot \begin{Bmatrix} \sigma_1 \\ \sigma_2 \\ \sigma_3 \\ \tau_{23} \\ \tau_{31} \\ \tau_{12} \end{Bmatrix} \tag{4}$$

where subscripts 1, 2, and 3 correspond to the main directions of the local reference frame of the hexagonal elements.

- E_1, E_2, and E_3 are, respectively, the longitudinal and transversal Young moduli;

- ν_{12} and ν_{21} are the in-plane Poisson ratios;
- ν_{31}, ν_{13}, ν_{23}, and ν_{32} are the out-of-plane Poisson ratios;
- G_{12} is the in-plane shear modulus;
- G_{13} and G_{13} are the out-of-plane shear moduli.

In order to respect symmetry in the matrix, it is necessary that

$$\frac{\nu_{12}}{E_1} = \frac{\nu_{21}}{E_2} \tag{5}$$

$$\frac{\nu_{13}}{E_1} = \frac{\nu_{31}}{E_3} \tag{6}$$

$$\frac{\nu_{23}}{E_2} = \frac{\nu_{32}}{E_3} \tag{7}$$

Given the high number of parameters, some assumptions are made. From experimental evidence, i.e., on the surface of the prosthetic, woven layers inclined ±45° are visible. Hence, it is assumed to have woven layers throughout the entire component. Thus, the in-plane Young moduli (E_1 and E_2) are assumed equal. As consequence, also ν_{13} and ν_{23} and G_{13} and G_{23} are considered equal [47,48]. Table 6 outlines the orthotropic material properties that best describe the dynamic behaviour of the component after an iterative tuning phase.

Table 6. Orthotropic material properties of the 3D model.

Property	Value
$E_1 = E_2$ [GPa]	11.0
E_3 [GPa]	42.3
G_{12} [GPa]	32.0
$G_{23} = G_{13}$ [GPa]	3.0
ν_{12}	0.6
$\nu_{13} = \nu_{23}$	0.2

The first six mode shapes (orthotropic material FEA) are displayed in Figure 9, while corresponding natural frequencies are compared to EMA ones in Table 7, which shows the MAC values computed for each mode shape as well. The mode shapes depicted in Figure 9 seem to match those observed in the experimental counterparts (in Figure 4). Specifically, the first, third, and fifth modes correspond to the first, second, and third bending moments in the XZ plane. The second and sixth modes affect the torsion of the distal area of the prosthetic, while the fourth mode affects the torsion of the socket area. The good agreement between the experimental and numerical mode shapes is also demonstrated by the evaluation of the MAC matrix. Indeed, as visible in Figure 8b, high diagonal values result in the MAC matrix of FEA and EMA comparison, as already obtained by the authors for other mechanical systems [51,52]. MAC index of the sixth mode shape falls below the above-mentioned threshold of 70%, probably because the simulation is not able to capture some major displacements in the toe area (see Figure 4f). Even natural frequencies are almost the same between EMA and FEA referring to the iso-frequency line of Figure 8. The real components turn out to be slightly stiffer than the orthotropic material model starting from the third mode shape.

Table 7. Natural frequencies and MAC values between FEA (orthotropic) and EMA results.

Mode n.	f_{FEA} [Hz]	f_{EMA} [Hz]	Mode Shape	MAC [%]
1	91.32	86.33	1st bending XZ	90.03
2	224.51	226.49	Torsion RZ/1st bending XY	79.91
3	236.92	275.25	2nd bending XZ	79.59
4	298.82	371.77	Torsion RZ/2nd bending XY	94.20
5	478.80	603.34	3rd bending XZ	76.74
6	643.30	735.60	Torsion RZ/3rd bending XY	60.56

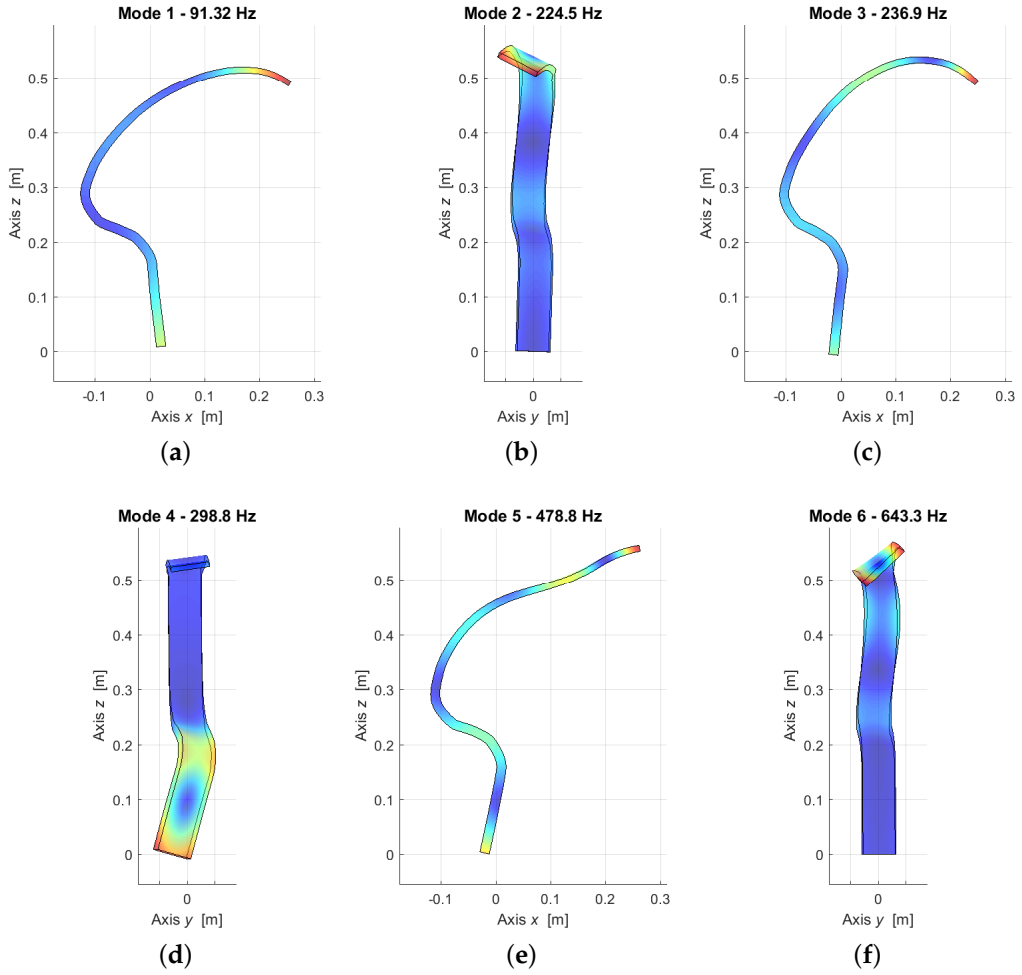

Figure 9. Mode shapes resulting from the simulation with orthotropic material properties.

4. Conclusions

In this research work, the dynamic modal behaviour of a lower limb blade prosthetic is investigated. Experimental natural frequencies, damping, and mode shapes of the system are evaluated up to 750 Hz. In agreement with the component geometry, which presents a cross-section much wider than thick, the principal mode shapes of the prosthetic are the bending in the main plane and the torsion along the profile. Furthermore, it appears reasonable that the first mode is the bending in the vertical plane, considering that the primary function of the leg prosthetic is the displacement along the vertical direction, promoting energy storage and release functionality, thus assisting athletes in achieving an efficient running gait.

From the experimental results obtained, the overall material characteristics of the component are extrapolated by comparing the FE simulations to the experimental outcomes. As a main result, the prosthetic cannot be modelled with isotropic material properties, and the

definition of orthotropic characteristics is necessary. Indeed, the actual component is in composite, specifically composed of carbon fibre layers, which adhere to the structural anisotropic characteristics. The assumption of isotropic material properties is not able to simulate the dynamic behaviour of the prosthesis. As a consequence, this study demonstrates that both geometry band material characteristics play a crucial role in the dynamic behaviour of the prosthetic. Thus, comprehensive insight of the dynamic behaviour of the prosthetic may contribute to further optimise the prosthetic performances, providing modifications in the manufacturing process.

In order to gain a wider understanding of the mechanical characteristics and dynamic behaviour of the component, static tests and loaded modal analyses may be performed to better simulate operating conditions.

Author Contributions: Conceptualization, C.B., L.D., A.D.V. and A.V.; methodology, C.B., L.D., A.D.V. and A.V.; software, C.B., L.D. and A.D.V.; validation, L.D., A.D.V. and A.V.; formal analysis, C.B., L.D., A.D.V. and A.V.; investigation, C.B., L.D. and A.D.V.; writing—original draft preparation, C.B., L.D. and A.D.V.; writing—review and editing, C.B., L.D., A.D.V. and A.V.; visualization, L.D. and A.D.V.; supervision, A.V. All authors have read and agreed to the published version of the manuscript.

Funding: This research received no external funding.

Institutional Review Board Statement: Not applicable.

Informed Consent Statement: Not applicable.

Data Availability Statement: Not applicable.

Acknowledgments: The authors wish to acknowledge Peter Slijkhuis, Director of Össur Academy, for providing the composite ESAR prosthetic Cheeta Xcel, and for his support during this research activity.

Conflicts of Interest: The authors declare no conflict of interest.

References

1. Houdijk, H.; Wezenberg, D.; Hak, L.; Cutti, A.G. Energy storing and return prosthetic feet improve step length symmetry while preserving margins of stability in persons with transtibial amputation. *J. Neuroeng. Rehabil.* **2018**, *15*, 76. [CrossRef]
2. Siddiqui, M.I.H.; Arifudin, L.; Alnaser, I.A.; Hassan, A.H.A.; Alluhydan, K. Static Behavior of a Prosthetic Running Blade Made from Alloys and Carbon Fiber. *J. Disabil. Res.* **2023**, *2*, 63–74. [CrossRef]
3. Hobara, H.; Baum, B.S.; Kwon, H.J.; Miller, R.H.; Ogata, T.; Kim, Y.H.; Shim, J.K. Amputee locomotion: Spring-like leg behavior and stiffness regulation using running-specific prostheses. *J. Biomech.* **2013**, *46*, 2483–2489. [CrossRef] [PubMed]
4. Srinivasan, V.; Govarthan, P.K.; Prakash, S.O.; Munirathinam, D. Composite blades for lower extremity amputees. In *IOP Conference Series: Materials Science and Engineering*; IOP Publishing: Bristol, UK, 2022; Volume 1258, p. 012044.
5. Wezenberg, D.; Cutti, A.G.; Bruno, A.; Houdijk, H. Differentiation between solid-ankle cushioned heel and energy storage and return prosthetic foot based on step-to-step transition cost. *J. Rehabil. Res. Dev.* **2014**, *51*, 1579–1590. [CrossRef]
6. Gürdal, Z.; Tatting, B.F.; Wu, C. Variable stiffness composite panels: Effects of stiffness variation on the in-plane and buckling response. *Compos. Part A Appl. Sci. Manuf.* **2008**, *39*, 911–922. [CrossRef]
7. Haberkern, H. Tailor-made reinforcements. *Reinf. Plast.* **2006**, *50*, 28–33. [CrossRef]
8. Shabana, Y.M.; Ibrahim, A.E.; Shehata, D.; Mohamed, S.; Gamal, A.; Mohamed, A.A.; Saleh, E.A.; Zeinhom, S.S.; Mahmoud, E.B.; Abdelaziz, M.R.; et al. Design and Simulation of Prosthetic Running Blade Using Functionality Graded Materials. In Proceedings of the 2022 4th Novel Intelligent and Leading Emerging Sciences Conference (NILES), Giza, Egypt, 22–24 October 2022; pp. 163–166.
9. Ottobock. Sportsline—Running Prostheses. Available online: https://www.ottobock.com/en-ie/sportsline (accessed on 4 July 2023).
10. Össur. Sport Solutions. Available online: https://www.ossur.com/en-us/prosthetics/sport-solutions (accessed on 4 July 2023).
11. Blatchford. BladeXT. Available online: https://www.blatchfordmobility.com/en-us/products/feet-ankles/bladext/ (accessed on 4 July 2023).
12. Laferrier, J.Z.; Gailey, R. Advances in lower-limb prosthetic technology. *Phys. Med. Rehabil. Clin.* **2010**, *21*, 87–110. [CrossRef]
13. Kumar, P.K.; Charan, M.; Kanagaraj, S. Trends and challenges in lower limb prosthesis. *IEEE Potentials* **2017**, *36*, 19–23. [CrossRef]
14. Bhatt, S.; Joshi, D.; Rakesh, P.K.; Godiyal, A.K. Advances in additive manufacturing processes and their use for the fabrication of lower limb prosthetic devices. *Expert Rev. Med. Devices* **2023**, *20*, 17–27. [CrossRef]
15. Asif, M.; Tiwana, M.I.; Khan, U.S.; Qureshi, W.S.; Iqbal, J.; Rashid, N.; Naseer, N. Advancements, trends and future prospects of lower limb prosthesis. *IEEE Access* **2021**, *9*, 85956–85977. [CrossRef]

16. Cavallaro, L.; Tessari, F.; Milandri, G.; De Benedictis, C.; Ferraresi, C.; Laffranchi, M.; De Michieli, L. Finite element modeling of an energy storing and return prosthetic foot and implications of stiffness on rollover shape. *Proc. Inst. Mech. Eng. Part H J. Eng. Med.* **2022**, *236*, 218–227. [CrossRef]
17. Dyer, B.T.; Sewell, P.; Noroozi, S. How should we assess the mechanical properties of lower-limb prosthesis technology used in elite sport?: An initial investigation. *J. Biomed. Sci. Eng.* **2013**, *6*, 116–123. [CrossRef]
18. Petrone, N.; Costa, G.; Foscan, G.; Gri, A.; Mazzanti, L.; Migliore, G.; Cutti, A.G. Development of Instrumented Running Prosthetic Feet for the Collection of Track Loads on Elite Athletes. *Sensors* **2020**, *20*, 5758. [CrossRef] [PubMed]
19. Dyer, B.T.; Sewell, P.; Noroozi, S. An investigation into the measurement and prediction of mechanical stiffness of lower limb prostheses used for running. *Assist. Technol.* **2014**, *26*, 157–163. [CrossRef]
20. Beck, O.N.; Taboga, P.; Grabowski, A.M. Characterizing the mechanical properties of running-specific prostheses. *PLoS ONE* **2016**, *11*, e0168298. [CrossRef] [PubMed]
21. Beck, O.N.; Taboga, P.; Grabowski, A.M. How do prosthetic stiffness, height and running speed affect the biomechanics of athletes with bilateral transtibial amputations? *J. R. Soc. Interface* **2017**, *14*, 20170230. [CrossRef]
22. Tryggvason, H.; Starker, F.; Lecomte, C.; Jonsdottir, F. Use of Dynamic FEA for Design Modification and Energy Analysis of a Variable Stiffness Prosthetic Foot. *Appl. Sci.* **2020**, *10*, 650. [CrossRef]
23. Jweeg, M.J.; Hassan, S.S.; Hamid, A.S. Impact testing of new athletic prosthetic foot. *Int. J. Curr. Eng. Technol.* **2015**, *5*, 121–127. [CrossRef]
24. Koehler-McNicholas, S.R.; Nickel, E.A.; Barrons, K.; Blaharski, K.E.; Dellamano, C.A.; Ray, S.F.; Schnall, B.L.; Hendershot, B.D.; Hansen, A.H. Mechanical and dynamic characterization of prosthetic feet for high activity users during weighted and unweighted walking. *PLoS ONE* **2018**, *13*, e0202884. [CrossRef]
25. Rigney, S.M.; Simmons, A.; Kark, L. Mechanical characterization and comparison of energy storage and return prostheses. *Med. Eng. Phys.* **2017**, *41*, 90–96. [CrossRef]
26. Hawkins, J.; Noroozi, S.; Dupac, M.; Sewell, P. Development of a wearable sensor system for dynamically mapping the behavior of an energy storing and returning prosthetic foot. *Meas. Sci. Rev.* **2016**, *16*, 174–182. [CrossRef]
27. Talla, H.K.; Oleiwi, J.K.; Hassan, A.K.F. Performance of Athletic Prosthetic Feet Made of Various Composite Materials with PMMA Matrix: Numerical and Theoretical Study. *J. Compos. Adv. Mater. Des Compos. Et Des Matériaux Avancés* **2021**, *31*, 257–264. [CrossRef]
28. Talla, H.K.; Hassan, A.K.F.; Oleiwi, J.K. Study the effect of reinforcing kevlar fibers with carbon fibers and glass fibers on the performance of the athletic prosthetic foot. *Basrah J. Eng. Sci.* **2022**, *22*, 41–48. [CrossRef]
29. *ISO 10328:2006*; Prosthetics: Structural Testing of Lower Limb Prostheses: Requirements and Test Methods. International Organization for Standardization: Geneva, Switzerland, 2006.
30. Noroozi, S.; Rahman, A.; Dupac, M.; Vinney, J. Dynamic characteristics of prosthetic feet: A comparison between modal parameters of walking, running and sprinting foot. In *Advances in Mechanisms Design: Proceedings of TMM 2012*; Springer: Dordrecht, The Netherlands, 2012; pp. 339–344. [CrossRef]
31. Noroozi, S.; Sewell, P.; Rahman, A.G.A.; Vinney, J.; Chao, O.Z.; Dyer, B. Modal analysis of composite prosthetic energy-storing-and-returning feet: An initial investigation. *Proc. Inst. Mech. Eng. Part P J. Sports Eng. Technol.* **2013**, *227*, 39–48. [CrossRef]
32. Noroozi, S.; Rahman, A.G.; Khoo, S.Y.; Zahedi, S.; Sewell, P.; Dyer, B.; Ong, Z.C. The dynamic elastic response to impulse synchronisation of composite prosthetic energy storing and returning feet. *Proc. Inst. Mech. Eng. Part P J. Sports Eng. Technol.* **2014**, *228*, 24–32. [CrossRef]
33. Noroozi, S.; Ong, Z.C.; Khoo, S.Y.; Aslani, N.; Sewell, P. Dynamic characterisation of Össur Flex-Run prosthetic feet for a more informed prescription. *Prosthetics Orthot. Int.* **2019**, *43*, 62–70. [CrossRef]
34. Nakayama, H.; Takahashi, Y.; Tanaka, K. Measurement of Dynamic Behavior of Running-Specific Prostheses by an Impact Test. *Proceedings* **2020**, *49*, 145. [CrossRef]
35. Vinney, J.; Noroozi, S.; Rahman, A.G.A.; Sewell, P.; Chao, O.Z.; Kuan, K.K.; Dupac, M. Analysis of Composite Prosthetic Energy-Storing-and-Returning (ESR) feet: A comparison between FEA and the experimental analysis. *Int. J. COMADEM* **2012**, *15*, 19–28.
36. Burnett, J.K.; Choi, Y.T.; Li, H.; Wereley, N.M.; Miller, R.H.; Shim, J.K. Vibration suppression of a composite prosthetic foot using piezoelectric shunt damping: Implications to vibration-induced cumulative trauma. *IEEE Trans. Biomed. Eng.* **2021**, *68*, 2741–2751. [CrossRef]
37. Pu, J.; Shi, Y.; Jia, Y. Energy Harvesting from Kinetics of Prosthetic Leg. In Proceedings of the 2019 19th International Conference on Micro and Nanotechnology for Power Generation and Energy Conversion Applications (PowerMEMS), Krakow, Poland, 2–6 December 2019; pp. 1–6. [CrossRef]
38. Pechrach, K.; Manoonpong, P.; Woegoetter, F.; Tungpimolrut, K.; Hatti, N.; Phontip, J.; Komoljindakul, K. Piezoelectric Energy Harvesting for Self Power Generation of Upper and Lower Prosthetic Legs. In Proceedings of the Piezo 2011 Conference, Sestriere, Italy, 28 Feburary–2 March 2011.
39. Jia, Y.; Wei, X.; Pu, J.; Xie, P.; Wen, T.; Wang, C.; Lian, P.; Xue, S.; Shi, Y. A numerical feasibility study of kinetic energy harvesting from lower limb prosthetics. *Energies* **2019**, *12*, 3824. [CrossRef]

40. Cheetah Xcel, Össur. Model Overview and Specifications. Available online: https://www.ossur.com/en-us/prosthetics/feet/cheetah-xcel (accessed on 15 June 2023).
41. Maia, N.M.M.; Montalvão e Silva, J.M. *Theoretical and Experimental Modal Analysis*; John Wiley & Sons Inc.: Hoboken, NJ, USA, 1997.
42. Peeters, B.; Van der Auweraer, H.; Guillaume, P.; Leuridan, J. The PolyMAX frequency-domain method: A new standard for modal parameter estimation? *Shock Vib.* **2004**, *11*, 395–409. [CrossRef]
43. Bonisoli, E.; Dimauro, L.; Venturini, S. Lupos: Open-source scientific computing in structural dynamics. In Proceedings of the 41st IMAC, A Conference and Exposition on Structural Dynamics, Austin, TX, USA, 13–16 February 2023.
44. Allemang, R.J. A correlation coefficient for modal vector analysis. In Proceedings of the 1st IMAC, Orlando, FL, USA, 8–10 November 1982; pp. 110–116.
45. Brigante, D.; Rainieri, C.; Fabbrocino, G. The role of the modal assurance criterion in the interpretation and validation of models for seismic analysis of architectural complexes. *Procedia Eng.* **2017**, *199*, 3404–3409. [CrossRef]
46. MSC Nastran. *Quick Reference Guide*; MSC Software Corporation: Newport Beach, CA, USA, 2016.
47. Gojny, K.; Dacko, A. Investigation of finite element (Fe) modelling of composite materials: Shell, solid and solid layered composite modelling–comparison of impact on simulation results. *Compos. Theory Pract.* **2021**, *21*, 29–39.
48. Guseinov, K.; Kudryavtsev, O.; Bezmelnitsyn, A.; Sapozhnikov, S. Determination of interlaminar shear properties of fibre-reinforced composites under biaxial loading: A new experimental approach. *Polymers* **2022**, *14*, 2575. [CrossRef] [PubMed]
49. Collins, L.N.; Roberts, S.A. Mesoscale simulation of woven composite design decisions. *arXiv* **2021**, arXiv:2104.13554.
50. Kaddaha, M.A.; Younes, R.; Lafon, P. Homogenization method to calculate the stiffness matrix of laminated composites. *Eng* **2021**, *2*, 416–434. [CrossRef]
51. Bonisoli, E.; Lisitano, D.; Dimauro, L. Experimental and numerical mode shape tracing from components to whole motorbike chassis. In Proceedings of the International Conference on Noise and Vibration Engineering—ISMA-USD2018, Leuven, Belgium, 17–19 September 2018; Moens, D., Desmet, W., Pluymers, B., Rottiers, W., Eds.; pp. 3597–3604.
52. Bonisoli, E.; Vella, A.D.; Venturini, S. Uncertainty effects on bike spoke wheel modal behaviour. In *Model Validation and Uncertainty Quantification*; Springer: Cham, Switzerland, 2023; Volume 3, pp. 111–123. [CrossRef]